Electrochemical Charge Storage Behavior of Various $NiCo_2S_4$ Hierarchical Microstructures

Xing Chen,[1,2] Chunfeng He,[1] Weiguo Wang,[1,2] Tian Bai,[1,2] Gaofei Xue,[1] and Meidan Ye[1,2,*]

[1] *Research Institute for Biomimetics and Soft Matter, Fujian Provincial Key Laboratory for Soft Functional Materials Research, Department of Physics, Xiamen University, Xiamen 361005, China*

[2] *Shenzhen Research Institute of Xiamen University, Shenzhen 518057, China*

(Received 22 December 2020; revised 23 March 2021; accepted 27 May 2021; published 16 June 2021)

The micro- and/or nanostructures of electrode materials play an essential role in their electrochemical performance, and the further understanding of their electrochemical behavior is vitally important for the rational design of high-performance electrochemical energy storage devices (EESDs). Herein, four types of $NiCo_2S_4$ hierarchical microstructures (HMSs; i.e., sphere-, hat-, brush-, and flowerlike HMSs) assembled from similar hollow nanoneedle building blocks are specially synthesized via a multistep strategy. A series of electrochemical analyses are performed to investigate the structure-activity relationship of these $NiCo_2S_4$ electrodes. The four $NiCo_2S_4$ electrodes all exhibit hybrid electrochemical characteristics combined with the adsorption and diffusion-controlled process of Faradaic redox reaction kinetics. Notably, the brushlike $NiCo_2S_4$ electrode displays the best specific capacitance (capacity) of 1684 F g^{-1} (234 mAh g^{-1}) at 1 A g^{-1}, and retains 91% of its initial performance after 10 000 cycles, which is mainly due to its well-ordered three-dimensional microstructure with sufficient surface reaction sites, fast charge transport, and efficient ion diffusion properties. The resulting hybrid supercapacitor delivers a high energy density of 2667 mWh kg^{-1} with a power density of 240 W kg^{-1} and is able to light up light-emitting diodes. Furthermore, the comparative electrochemical analysis of dynamic responses in different electrodes is helpful to further understand their charge-discharge mechanism and provide basic guidance to fabricate efficient electrodes for EESDs.

DOI: 10.1103/PhysRevApplied.15.064042

I. INTRODUCTION

Increasingly, the depletion of fossil fuels and the deteriorating ecological environment are forcing human beings to search extensively for alternative clean energy and advanced energy storage devices [1,2]. Electrochemical energy storage systems [e.g., supercapacitors (SCs) and lithium-ion batteries] show great potential in the power supply of portable electronics and vehicles owing to their high charge-discharge efficiency, long cycle life, and low maintenance cost [3–6]. There are various factors (e.g., porosity of active materials [7,8], and composition of electrolytes [9]) that affect the charge storage behavior and performance of electrochemical energy storage devices (EESDs). The exploitation of electrode materials with highly efficient, cheap, and stable characteristics is widely considered to be an effective strategy to fabricate high-performance EESDs [10–12]. Notably, the electrochemical charge storage behavior of electrode materials differs significantly between SCs and batteries [1]. In SCs, the electrical charges are stored in a Helmholtz double layer at the electrode-electrolyte interface without Faradaic reactions (i.e., electrical double layer capacitance), or via redox reactions with the Faradaic charge-transfer process on the surface or near the surface of electrodes without ion diffusion into the bulk electrode materials (i.e., pseudocapacitance). Charge storage in batteries is realized through the reversible Faradaic reactions or intercalation processes inside the bulk electrode materials and electrolyte. Phase transformation of the active materials occurs in batteries during the Faradaic charge storage processes, leading to the presence of obvious redox peaks in cyclic voltammograms (CVs; versus near-rectangular shapes or broadened peaks in CVs for SCs) and distinct plateaus in galvanostatic charge-discharge (GCD) profiles (versus quasitriangular shapes in GCD profiles for SCs) [13]. In essence, the intrinsic reaction kinetics of the Faradaic processes in batteries are dominated by the diffusion-controlled redox process (i.e., $I \propto v^{1/2}$, where I is the current and v is the scan rate in the CVs), while the reaction kinetics of pseudocapacitance follow the surface-controlled electrochemical process (i.e., $I \propto v$) [1]. Thus, it is necessary to further understand the physical and chemical characteristics of electrochemical charge storage processes in order to

*mdye@xmu.edu.cn

precisely assess and select the electrode active materials for EESDs.

To date, various nanostructured electrode materials, such as carbon-based materials (e.g., carbon nanotubes, nanofibers, porous structures, and graphene) [14–16], metal oxides (e.g., MnO_2, Co_3O_4, and $NiCo_2O_4$) [17, 18], metal sulfides (e.g., $NiCo_2S_4$, Co_9S_8, and NiS) [19], conductive polymers (e.g., polypyrrole and polyaniline) [20], metal nitrides and carbides (e.g., MXene) [21], and their composites [22–24], have been rapidly developed for EESDs in recent years. With the increasing exploitation of nanostructured electrodes in EESDs, the boundary between pseudocapacitors and batteries becomes indistinct. The same material can exhibit capacitive or battery-like behavior, largely depending on the electrode structural design and charge storage of guest ions [25,26]. For example, transition metal sulfides have been favored by many researchers for applications in SCs, which usually possess more complex valence states, larger lattice sizes, and higher electrical conductivity than their oxide counterparts, leading to rich redox reactions and high electrochemical activity in electrochemical processes [27–29]. It is found that metal sulfide materials frequently show hybrid charge storage behavior in electrochemical processes [23, 27–30]. Thus, it is important to differentiate the capacitive and diffusion-controlled contribution of metal sulfide electrodes in order to determine whether the capacitive behavior is dominant in the electrodes.

For metal sulfides, much effort has been focused on tuning their chemical compositions and micro- and/or nanostructures [31,32]. The different geometries of nanostructured electrodes have a remarkable impact on the charging dynamics of the macroscopic SCs [33]. A variety of architectures, including zero-dimensional (0D) nanoparticles [34,35], one-dimensional (1D) nanotubes, nanowires, and nanofibers [36,37], two-dimensional (2D) nanosheets [38,39], and three-dimensional (3D) hierarchical structures [40,41], have been developed for high-performance SCs. In particular, 3D hierarchical structures assembled by 0D, 1D, or 2D nanostructured building blocks exhibit superior electrochemical activity, mainly due to the integrated advantages (e.g., sufficient reaction sites, fast electron transport, and effective ion diffusion properties) of nanostructured building blocks for hierarchical frameworks. Thus, many studies have been devoted to the construction of hierarchical structures for effective electrodes [28,30,42,43]. However, the relationship between the hierarchical structures and the charging dynamics of electrodes is poorly understood. Furthermore, there are few works related to comparative studies of the charge storage behavior of different hierarchical structures of metal sulfides in the electrochemical processes.

Herein, four kinds of $NiCo_2S_4$ electrodes with sphere-, hat-, brush-, and flowerlike hierarchical microstructures (HMSs) assembled from many similar hollow nanoneedles are specifically synthesized via a multistep method. Related electrochemical analysis is carried out to deeply understand their electrochemical behavior based on different hierarchical architectures. The well-arranged brushlike $NiCo_2S_4$ HMS with a large surface area, fast charge transport channels, and rich ion diffusion paths displays the best electrochemical charge storage.

II. RESULTS AND DISCUSSION

As illustrated in Fig. S1 [44] and Fig. 1, the synthesis of four types of $NiCo_2S_4$ HMSs (i.e., sphere-, hat-, flower-, and brushlike HMSs), which are all self-assembled from many similar hollow nanoneedles, is successfully realized via a multistep strategy, mainly including electrostatic spinning, hydrothermal, and sulfuration processes. In particular, these four kinds of $NiCo_2S_4$ HMSs are all assembled from hollow nanoneedles. The formation mechanism of the hollow nanoneedles is associated with the nanoscale Kirkendall effect. In brief, during the first hydrothermal process, the Ni and Co precursors are formed as the nanoneedle templates. Then, in an early stage of the second hydrothermal process, $NiCo_2S_4$ is first grown on the surface of the nanoneedle templates. Next, the nickel and cobalt ions at the center of nanoneedles gradually diffuse to the surface of the templates and then react with sulfur ions to form $NiCo_2S_4$. As the reaction time increases, the nickel and cobalt ions at the center of the nanoneedle templates are exhausted and other species (e.g., Cl^-) dissolve in the hydrothermal solution, consequently resulting in the hollow nanoneedles [28,45,46]. Moreover, electrospun polyacrylonitrile nanofibers (PAN NFs) with diameters of about 250 nm and lengths of hundreds of micrometers [Figs. 1(c), 1(d) and Fig. S2 [44]] are employed to effectively assist the well construction of the brush- and flowerlike $NiCo_2S_4$ HMSs. Without the participation of PAN NFs, a spherelike $NiCo_2S_4$ HMS [Fig. 1(a); versus the brushlike HMS] is obtained, while a hatlike $NiCo_2S_4$ HMS [Fig. 1(b); versus the flowerlike HMS] is formed with the addition of NH_4F. As observed in Figs. 1(e)–1(h), the hundreds-of-micrometer-long brushlike HMS is self-assembled from numerous hollow nanoneedles (diameters ∼150 nm) vertically grown on the outer wall of a backbone (diameter ∼500 nm). It is revealed that the introduction of PAN NFs can induce the well-aligned growth of nanoneedles along the NFs to build a brushlike architecture. However, the addition of NH_4F in the hydrothermal precursor can dramatically influence the reaction conditions (e.g., acidity and ion interaction) and thus lead to the formation of the flowerlike HMS [Figs. 1(i)–1(l)], which is more compact and aggregated than the brushlike one. These $NiCo_2S_4$ HMSs show the spinel crystal phase (Joint Committee on Powder Diffraction Standards No. 20-0782; Fig. S3 [44]), and the brushlike $NiCo_2S_4$ HMS has a

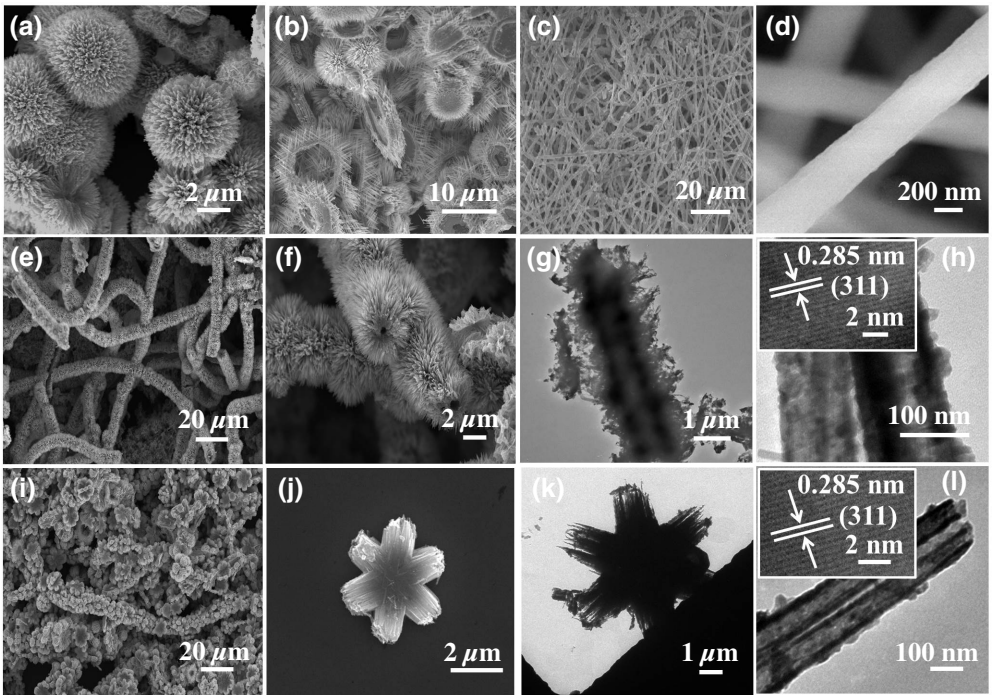

FIG. 1. (a)-(f), (i) and (j) SEM images, and (g), (h), (k) and (l) TEM images: (a) spherelike $NiCo_2S_4$, (b) hatlike $NiCo_2S_4$, (c) and (d) PAN NFs, (e)-(h) brushlike $NiCo_2S_4$ and (i)-(l) flowerlike $NiCo_2S_4$.

larger specific surface area and more mesoporous pores (Fig. S4 [44]; 20.1 m^2 g^{-1} vs. 6.8 m^2 g^{-1} for the flowerlike $NiCo_2S_4$ HMS), which provide more active sites and speed up ion transfer for the electrochemical charge storage process. As shown in Table SI [44], the four kinds of $NiCo_2S_4$ electrodes have different morphologies, diameters, lengths or thicknesses, and conductivities, which lead to their performance differences.

To investigate the electrochemical behavior of these four kinds of $NiCo_2S_4$ electrodes, CV, GCD, and electrochemical impedance spectroscopy (EIS) tests are performed in a three-electrode system. CV is a powerful technique to differentiate the electrochemical characteristics and evaluate the charge storage performance of electrodes. As shown in Figs. 2(a)–2(d), CV curves with different potential ranges at scan rates from 10 to 50 mV s^{-1} are measured for different $NiCo_2S_4$ electrodes. The features of CV curves with obvious redox peaks reveal the presence of Faradaic redox reactions between Ni^{2+} and/or Ni^{3+} and Co^{2+} and/or Co^{3+} and the hybrid electrochemical characteristics of these $NiCo_2S_4$ HMSs. In the KOH aqueous electrolyte, the correlated Faradaic reactions of $NiCo_2S_4$ can be described as follows:

$$NiCo_2S_4 + OH^- + H_2O \leftrightarrow NiSOH + 2CoSOH + e^- \quad (1)$$

$$CoSOH + OH^- \leftrightarrow CoSO + H_2O + e^-. \quad (2)$$

In these hierarchical mesoporous $NiCo_2S_4$ electrodes, the diffusion rate of species (e.g., OH^-) into the pores of the electrodes is feasibly controlled by the scan rate (v) during the CV measurement. Under a low v, the species can fully access the pores and thus both diffusion-controlled and capacitive Faradaic processes occur simultaneously. At a high v, the species diffusion is limited and the battery-like Faradaic electrochemical process is restricted to some extent. In particular, the structural difference results in some distinctive features of CV curves for these $NiCo_2S_4$ electrodes [Fig. 2(e)]. For scan rates from 10 to 50 mV s^{-1}, the shapes of the CV curves for the sphere-, brush-, and hatlike $NiCo_2S_4$ electrodes remain consistent, suggesting a major contribution from capacitive processes or efficient ion diffusion throughout the electrodes. Furthermore, the spherelike $NiCo_2S_4$ electrode exhibits a higher electrochemical current than the hatlike one [Figs. 2(a) and 2(c)]. The secondary construction of brush- and flowerlike $NiCo_2S_4$ electrodes with chain hierarchical architectures substantially improves the electrochemical charge storage performance of brush- and flowerlike $NiCo_2S_4$ electrodes [Figs. 2(b) and 2(d)], and the brushlike $NiCo_2S_4$ electrode possesses the best energy storage capability with the highest electrochemical current [Fig. 2(e)]. Notably, the position of redox peaks for each $NiCo_2S_4$ electrode is slightly different [Figs. 2(a)–2(d)]. It is indicated that the microstructures of the electrodes significantly influence their electrochemical processes and performance.

Moreover, the differentiation and quantitative calculation of capacitive (surface-controlled) and diffusion-controlled electrochemical behavior of the $NiCo_2S_4$ electrodes are further carried out based on the CV data. The hybrid electrochemical behavior of electrodes can be

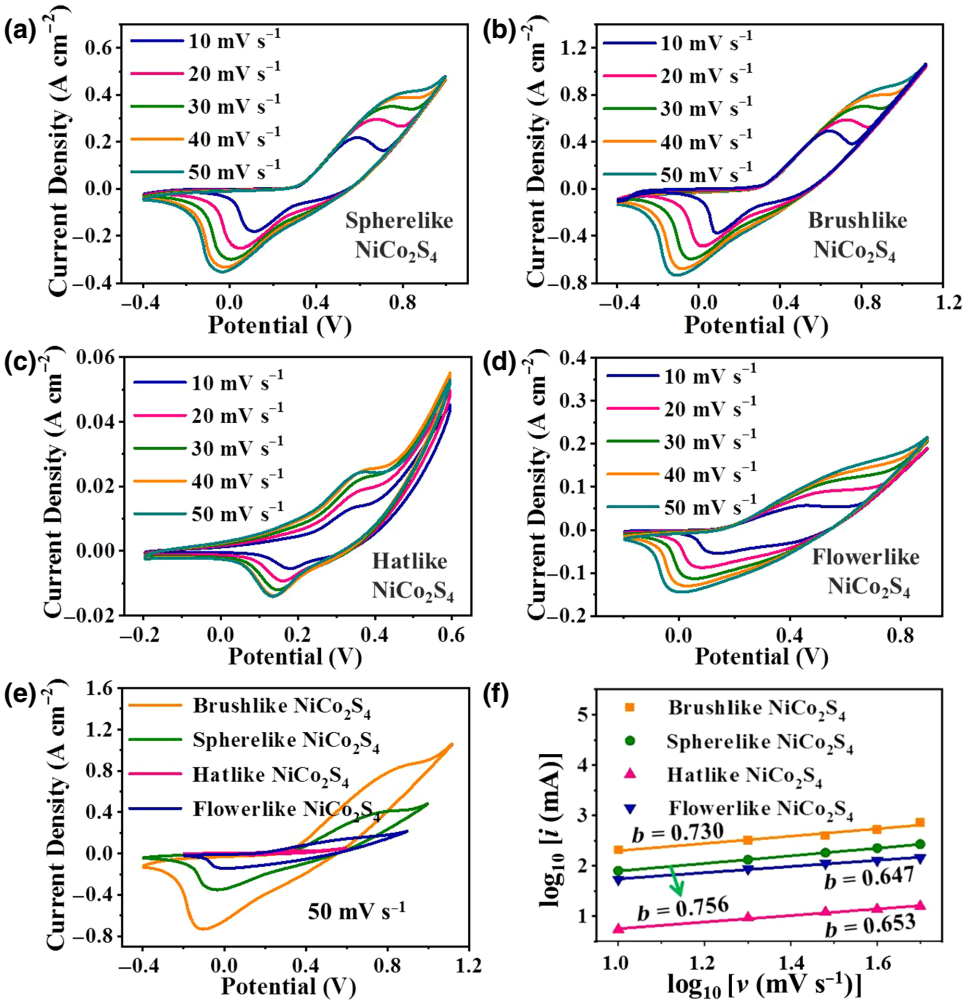

FIG. 2. (a)–(e) CV curves at different scan rates, and (f) the values of b obtained from the CV curves for the four $NiCo_2S_4$ electrodes.

analyzed using the following [1,47]:

$$i = av^b, \tag{3}$$

where i represents the current of the CV measurements, v is the scan rate, a and b express the tunable parameters, and b offers information about the mechanism of electrochemical charge storage.

For pseudocapacitive materials, the electrochemical processes are mainly dominated by the capacitive behavior and the current varies linearly with the sweep rate ($b = 1$) [1,13]

$$i = av, \tag{4}$$

$$|i| = ACv, \tag{5}$$

where A is the surface area of the active material, and C is the capacitance.

For batterylike materials, the Faradaic redox reactions of electrodes are dominated by the diffusion-controlled process, and the peak current of a reversible redox reaction is proportional to $v^{1/2}$ ($b = 0.5$) [1,13]

$$i = av^{1/2}, \tag{6}$$

$$i = nFAC^*D^{1/2}v^{1/2}\left(\frac{nF}{RT}\right)^{1/2}\pi^{1/2}\chi(bt), \tag{7}$$

where n is the number of electrons transferred per mole, F is the Faraday constant (96 485 C mol^{-1} e^{-1}), C^* represents the concentration of the species, D is the diffusion coefficient, R is the ideal gas constant (8.314 J K^{-1} mol^{-1}), T is the reaction temperature, t is time, and the χ function at any given point on the wave is a pure number. Thus, for the electrode with hybrid electrochemical behavior, the whole current can be described as follows:

$$i = i_{\text{pseudocapacitance}} + i_{\text{battery}} = k_1 v + k_2 v^{1/2}, \tag{8}$$

$$\frac{i}{v^{1/2}} = k_1 v^{1/2} + k_2, \tag{9}$$

where k_1 and k_2 are the capacitive and diffusion-controlled contributions, respectively. Accordingly, the kinetic information about pseudocapacitive and batterylike behavior of

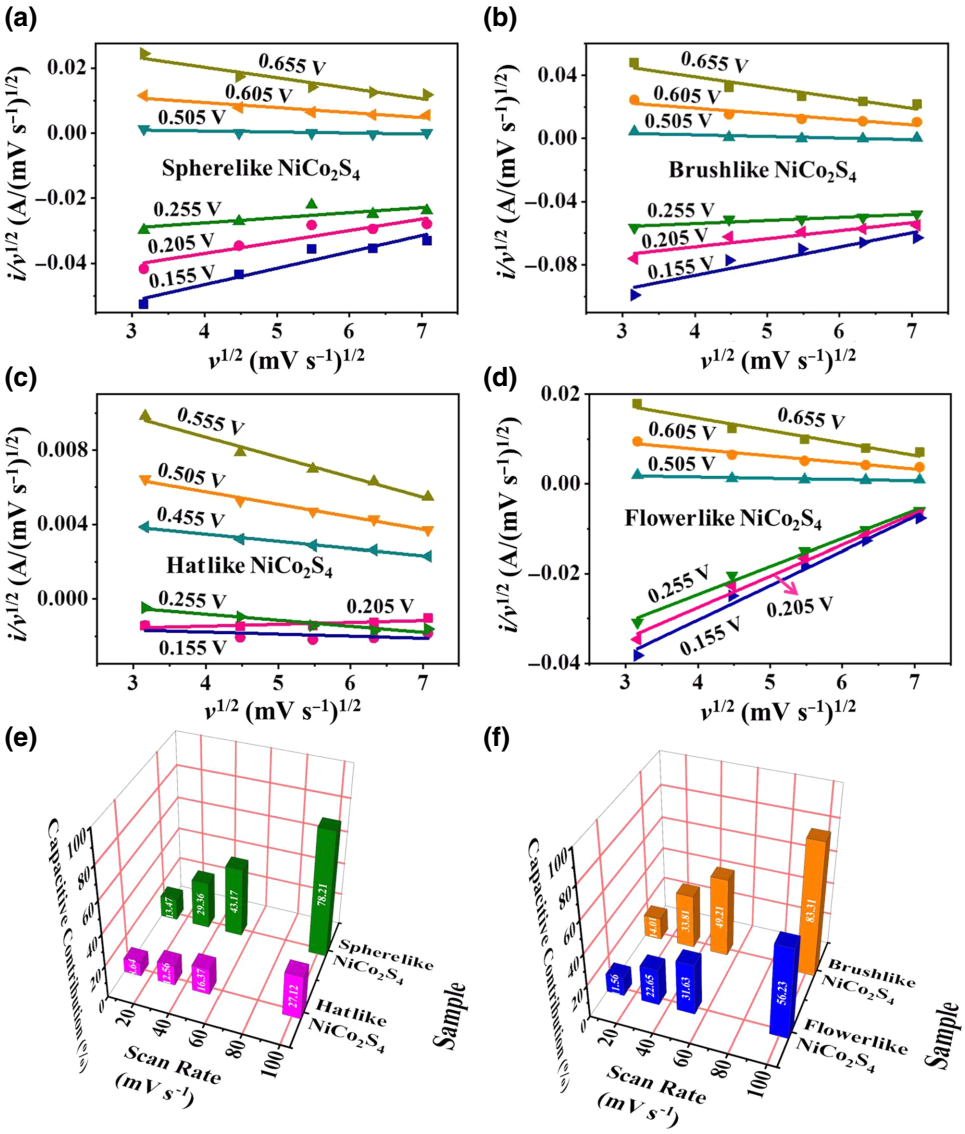

FIG. 3. (a)–(d) The values of k_1 obtained from CV curves at different potentials, and (e) and (f) the percentages of capacitive contribution at different scan rates for the four $NiCo_2S_4$ electrodes.

electrodes can be differentiated from the CV data and the capacitive contributions of different electrodes can also be evaluated (Fig. 3). As shown in Fig. 2(f), the b values can be roughly estimated by the linear plot of log i versus log v, and it can be seen that all $NiCo_2S_4$ electrodes exhibit a hybrid charge storage mechanism (i.e., $i \sim v^{0.5<b<1}$). The sphere- and brushlike electrodes have slightly higher b values with more capacitive behavior and thus a higher capacitive contribution for the charge storage performance [Figs. 3(e) and 3(f)]. In addition, their capacitive contributions all increase with increasing scan rates. This again indicates that the electrodes mainly present diffusion-controlled behavior with high energy densities at low scan rates, while they may display obvious capacitive behavior with high charge storage kinetics at high scan rates.

The GCD tests are also performed to analyze the energy storage performance and cycling stability of the $NiCo_2S_4$ electrodes. The GCD curves within a potential window of 0−0.5 V at current densities from 0.5 to 5 A g^{-1} are measured for different $NiCo_2S_4$ HMS electrodes. The GCD curves of these $NiCo_2S_4$ electrodes display nonlinear charge-discharge curves with tiny sloping voltage plateau regions (Fig. 4), suggesting that they experience some diffusion-controlled electrochemical reactions and have hybrid electrochemical properties. Notably, the current density for the GCD tests also influences the electrochemical behavior. At a low current density, both the inner and outer reaction sites of electrodes can be accessible to the species from electrolyte, and thus both the adsorption and diffusion-controlled Faradaic processes can occur, resulting in high values for the specific capacitance and capacity of the electrodes. However, at a high current density, only the outer surface areas of electrodes can be effectively used and the surface and/or near surface Faradaic process

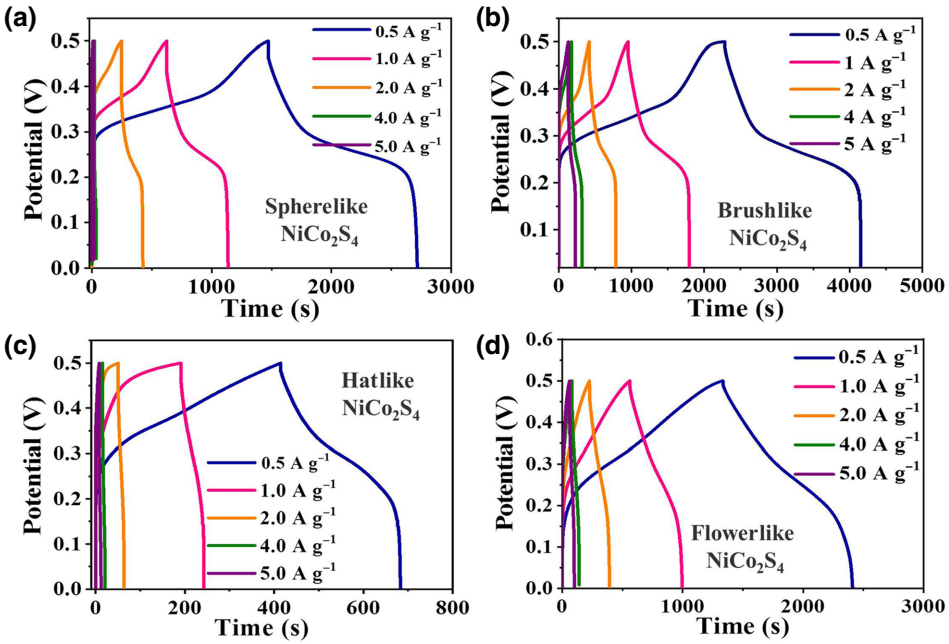

FIG. 4. GCD curves at different current densities for the four $NiCo_2S_4$ electrodes.

will dominate the specific capacitance and capacity of the electrodes.

In addition, the rate capability of electrodes can be evaluated by testing their specific capacitance or capacity under different current densities. The mass specific capacitance (C_1, F g^{-1}) or capacity (C_2, mAh g^{-1}) of the $NiCo_2S_4$ electrodes can be calculated through the corresponding GCD profiles via the following:

$$C_1 = \frac{It}{m\Delta U}, \tag{10}$$

$$C_2 = \frac{It}{3.6m}, \tag{11}$$

where I (A) is the discharge current, t (s) is the discharge time, ΔU (V) is the potential difference and m (g) is the mass of the active material. As shown in Fig. 5(a), the brushlike $NiCo_2S_4$ electrode displays the best specific capacitance (capacity) of 1684 F g^{-1} (234 mAh g^{-1}) at 1 A g^{-1}, which remains at 980 F g^{-1} (136 mAh g^{-1}) even at 5 A g^{-1}, indicating a performance retention of 58% (vs. 46% for the flowerlike one, 41% for the hatlike one, and 7% for the spherelike one). Moreover, the cycling stability of electrodes can be studied by continuously measuring GCD cycles at a fixed current density for thousands of cycles. The brushlike $NiCo_2S_4$ electrodes can maintain 91% of their initial performance after 10 000 cycles at 10 A g^{-1} [Fig. 5(b)]. In addition, the Coulombic efficiency (CE) of electrodes can also be obtained from the GCD profiles according to the following equation:

$$\text{CE}\ (\%) = \frac{\Delta q_d}{\Delta q_c} \times 100 = \frac{\int_0^{t_d} i_d dt}{\int_0^{t_c} i_c dt} \times 100, \tag{12}$$

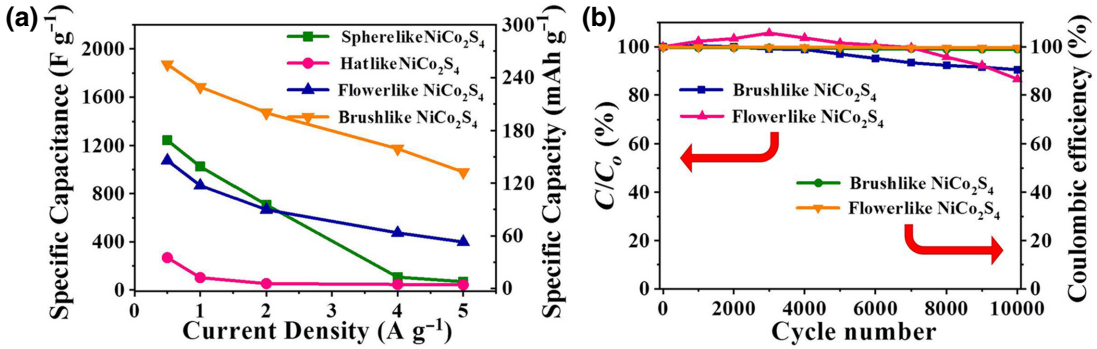

FIG. 5. (a) Specific capacitance/capacity values derived from the GCD curves at different current densities for the four $NiCo_2S_4$ electrodes, respectively. (b) Cycling stability and Coulombic efficiency within 10 000 cycles at 10 A g^{-1} for the brush- and flowerlike, respectively.

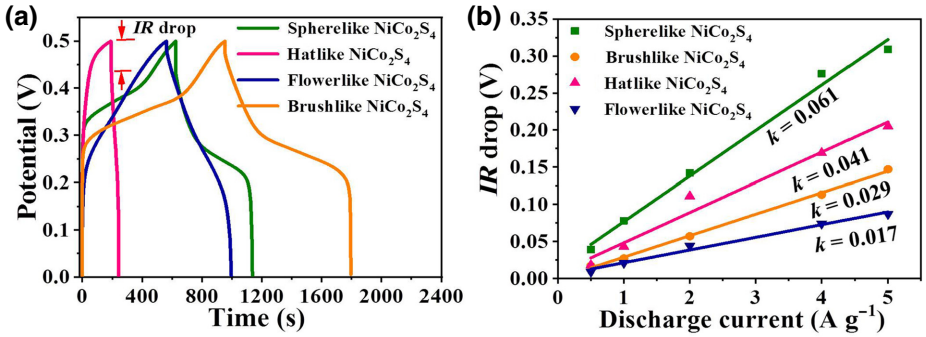

FIG. 6. (a) GCD curves at a current density of 1 A g^{-1}, and (b) voltage drop (*IR* drop) as a function of discharge current for the four $NiCo_2S_4$ electrodes.

where q_d and q_c represent the charges extracted from and inserted into the electrodes, respectively, t_d and t_c represent the discharging and charging times, respectively, and i_d and i_c represent the discharging and charging currents, respectively. Thus, the brushlike $NiCo_2S_4$ electrodes also exhibit a high CE of nearly 100% [Fig. 5(b)]. Moreover, compared with other nickel cobalt sulfide electrodes, they also have quite excellent performance (Table SII [44]). The high rate capability, cycling stability, and CE of the brushlike $NiCo_2S_4$ electrode is mainly due to its high charge transfer kinetics benefiting from the special well-defined 3D hierarchal architecture assembled from lots of 1D hollow nanoneedles.

Moreover, based on the GCD curves, a direct voltage drop (*IR* drop) can be observed at the beginning of the discharge curve [inset in Fig. 6(a)], which is largely associated with the equivalent series resistance (ESR) of the system, mainly including the internal resistance of the electrode, the contact resistance between the electrolyte and the electrode, the bulk solution resistance, and the ion-migration resistance in the electrode [1,13]. The *IR* drop is linear with the discharge current density [Fig. 6(b)], and the slope (k) of the fitting curve approximately reveals the ESR of the system, i.e., the larger k becomes, the higher the overall resistance of the system [30]. Thus, it is demonstrated that the brush- and flowerlike $NiCo_2S_4$ electrodes have smaller k values than those of the sphere- and hatlike $NiCo_2S_4$ electrodes, suggesting that the reassembly of the chain hierarchical structures of $NiCo_2S_4$ is beneficial for improving the charge dynamics in the system.

In addition, the EIS tests are conducted to explore the internal resistance, charge transfer characteristics, and ion diffusion process of the $NiCo_2S_4$ electrodes. As shown in Fig. 7, the resulting Nyquist plot is composed of a semicircular curve associated with the Faradaic interfacial charge-transfer resistance (R_{ct}) at high frequencies and a linear curve related to the Warburg resistance (Z_W) at low frequencies [27–29]. The corresponding equivalent circuit can be found in the inset of Fig. 7. The total impedance of the electrode with hybrid electrochemical behavior can be expressed as [1]

$$Z_{\text{Total}} = Z_{R_s} + \frac{1}{Z_{\text{CPE}} + [1/(Z_{R_{\text{ct}}} + Z_W)]}, \tag{13}$$

$$Z_{\text{CPE}} = a^{-1}(j\omega)^{-n'}, \tag{14}$$

$$j^{n'} = \cos\left(\frac{\pi}{2}n'\right) + j\sin\left(\frac{\pi}{2}n'\right); j = \sqrt{-1}, \tag{15}$$

$$\omega^{n'} = \frac{1}{R_{\text{ct}}C_{\text{CPE}}}, \tag{16}$$

$$Z_W = \frac{\sigma}{\sqrt{\omega}} - j\frac{\sigma}{\sqrt{\omega}}, \tag{17}$$

$$\sigma = \frac{RT}{n^2F^2A\sqrt{2}}\left(\frac{1}{D_o^{1/2}C_o^*} + \frac{1}{D_r^{1/2}C_r^*}\right), \tag{18}$$

$$Z_{\text{Total}} = R_s + \left\{a\omega^{n'}\left[\cos\left(\frac{\pi}{2}n'\right) + j\sin\left(\frac{\pi}{2}n'\right)\right] + \left[R_{\text{ct}} + \frac{\sigma}{\sqrt{\omega}} - j\frac{\sigma}{\sqrt{\omega}}\right]^{-1}\right\}^{-1}, \tag{19}$$

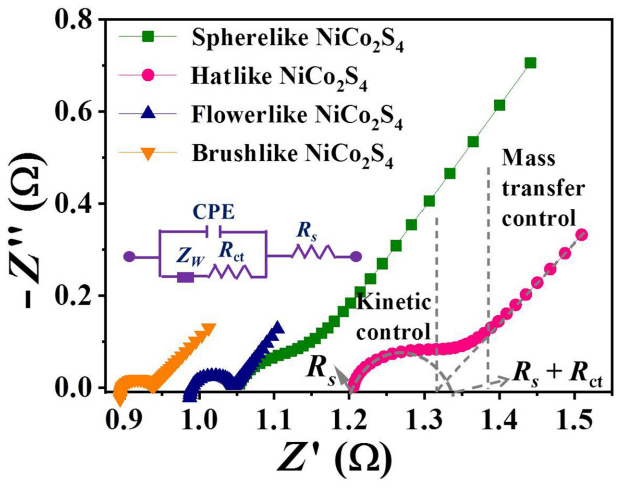

FIG. 7. Nyquist plots (inset is the corresponding equivalent circuit) for different $NiCo_2S_4$ electrodes.

where R_s is the ESR consisting of the electrolyte resistance, the inherent resistance of the electrode active materials,

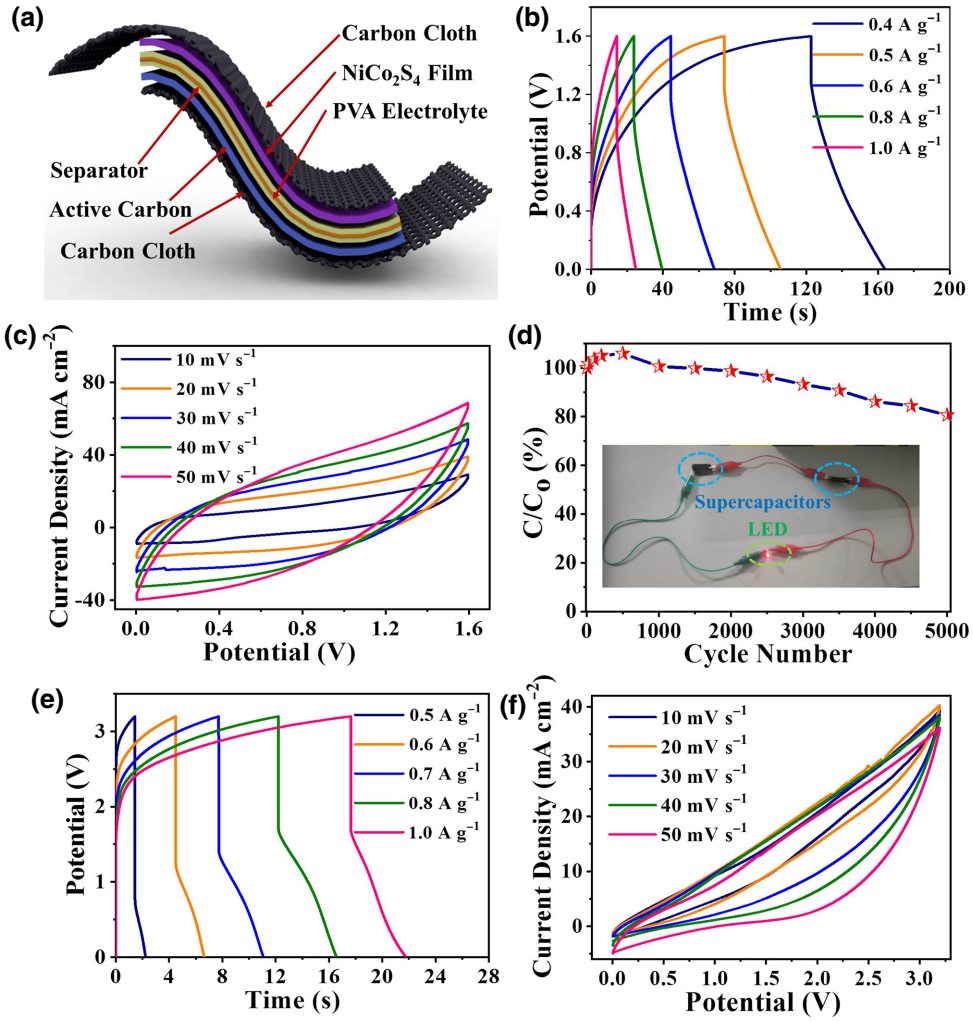

FIG. 8. (a) Schematic illustration and (b)–(d) electrochemical performance of the asymmetric supercapacitor based on the brushlike $NiCo_2S_4$ electrode: (b) GCD curves at different current densities, (c) CV curves at different scan rates, and (d) cycling stability at 10 A g^{-1} (inset is the picture of the supercapacitors lighting a LED). (e) GCD and (f) CV curves of two asymmetric supercapacitors in series.

and the contact resistance between the electrode active materials and the current collectors, CPE is a constant phase element to replace a double layer capacitor ($C_{\rm dl}$) for hybrid electrodes, D_o and D_r are the diffusion coefficients of the Oxidant and Reductant species, C_o^* and C_r^* represent the concentrations of the Oxidant (Ox) and Reductant species, n describes the number of electrons transferred per mole, F is the Faraday constant, R is the ideal gas constant, T is the temperature, ω is the angular frequency ($\omega = 2\pi f$), where f is the frequency, a represents the frequency-independent constant associated with the surface properties of electrodes, n describes the number of electrons transferred per mole. The exponent n' is derived from the slope of log Z versus log f ($-1 \le n' \le 1$). Accordingly, when the charge transfer process is much faster ($R_{\rm ct}$ is low) than the mass transfer process, the Nyquist plot just has a Warburg element consisting of a diagonal line with a 45° slope; in contrast, when the Faradaic reactions are kinetically sluggish ($R_{\rm ct}$ is high) the semicircular region will dominate the Nyquist plot while the Warburg line will not be apparent [1,13]. Therefore, the EIS curves of these four $NiCo_2S_4$ electrodes reveal their hybrid characteristics combining with the diffusion process and the redox reaction kinetics. The brush- and flowerlike $NiCo_2S_4$ electrodes have relatively small R_s and $R_{\rm ct}$ values compared with those of the sphere- and hatlike $NiCo_2S_4$ electrodes (Fig. 7 and Table SIII [44]). This is mainly because their electrode active materials have effective hierarchical structures (i.e., each nanoneedle building block is well connected in a chain for the brushlike electrode, while many nanoneedles are tightly interlaced to form flowerlike structures), which will have relatively lower inherent resistance and more efficient charge transfer in the electrode-electrolyte interface.

In order to further study the practical application of $NiCo_2S_4$ HMS electrodes, an asymmetric supercapacitor (ASC) is fabricated by employing the brushlike $NiCo_2S_4$ HMS as the cathode electrode and activated carbon as the anode electrode with the polyvinyl alcohol (PVA) gel electrolyte containing KOH [Fig. 8(a)]. The GCD curves of the resulting ASC at different current densities have obvious

voltage drops [V_R, Fig. 8(b)], indicating the large contact resistance between the electrode and the quasi-solid-state gel electrolyte.

$$V = V_R + V_C = iR + \frac{q_{\text{total}}}{C}, \tag{20}$$

where V_C is the potential across the device and q_{total} is the total charge. Owing to the sluggish ion diffusion of the gel electrolyte, the batterylike Faradaic processes are significantly limited. The rectanglelike CV curves of the ASC indicate the reversible Faradaic reactions and ideal capacitive properties of the device [Fig. 8(c)]. The mass energy density and power density of the ASC can be calculated using the following equations:

$$E = \frac{\int I \times U(t)dt}{3.6m}, \tag{21}$$

$$P = \frac{E}{t} \times 3600, \tag{22}$$

where $U(t)$ is the potential (V), E is the mass energy density (mWh g^{-1}), and P is the mass power density (mW g^{-1}). The ASC exhibits an energy density of 2666.7 mWh kg^{-1} at a power density of 240 W kg^{-1}, and can retain about 81% of the initial performance after 5000 continuous charging-discharging cycles at a current density of 1 A g^{-1} [Fig. 8(d)]. Two ASC devices connected in series are able to power a red light-emitting diode [LED; inset in Fig. 8(d)]. Figures 8(e)–8(f) show the GCD and CV curves of the connected ASCs. This result proves that the $NiCo_2S_4$ electrodes can be applied as the positive electrode materials of SCs.

Thus, the charge storage behavior of the hierarchical $NiCo_2S_4$ electrodes during electrochemical processes is complicated. There are many factors that affect the charge dynamics and ion diffusion across the electrode and the interface between electrode and electrolyte. The micro- or nanostructures have a significant impact on the electrochemical behavior of electrodes. As illustrated in Fig. 9, the excellent electrochemical performance of the brushlike $NiCo_2S_4$ HMS can be reasonably interpreted as follows: (1) the hollow structures of nanoneedles have large specific surface areas and uniform mesopores, which provide sufficient active sites for Faradaic reactions and rich channels for ion transport, (2) the uniform growth of active substances on the surface of PAN NFs gives the electrode great mechanical strength and electrical conductivity, and (3) the well-aligned and dense structures of the brushlike HMS make the active material less likely to collapse and aggregate during electrochemical reactions.

Moreover, as shown in Figs. S5–S8 [44], nitrogen has a uniform distribution among the brush- and flowerlike structures, suggesting that during the hydrothermal

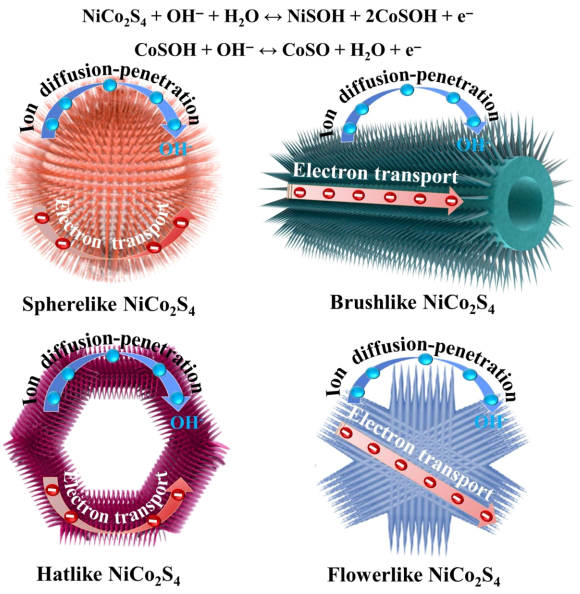

FIG. 9. Schematic diagrams of the ion diffusion and charge transport in the electrochemical process for different $NiCo_2S_4$ electrodes.

reaction at high temperatures, the brush- and flowerlike $NiCo_2S_4$ structures are probably doped with a small amount of nitrogen due to the addition of PAN NFs. The N-doping can create specific defect structures, which not only provide more active sites for redox reactions, but also improve the electrical conductivity of samples [48].

III. CONCLUSIONS

In summary, a comparative study on the electrochemical charge storage behavior of various $NiCo_2S_4$ electrodes with different HMSs is carried out. A series of electrochemical measurements demonstrate that all of the four $NiCo_2S_4$ electrodes exhibit hybrid capacitive and batterylike electrochemical behavior, and the well-aligned and highly ordered HMSs give the electrodes sufficient surface reaction sites, effective charge transport paths, and abundant ion diffusion channels, consequently yielding excellent electrochemical energy storage capability. That is, the well-arranged brushlike $NiCo_2S_4$@PAN electrode renders a set of outstanding electrochemical performance (e.g., high specific capacity of 234 mA h g^{-1} at 1 A g^{-1} and excellent cycling stability with 91% capacity retention after 10 000 cycles). The resulting asymmetric supercapacitors exhibit a high energy density of 2666.7 mWh kg^{-1} at a power density of 240 W kg^{-1}, and great cycling stability of 81% over 5000 cycles. In addition, the detailed electrochemical analysis is useful to deeply understand the hybrid electrochemical behavior of electrodes.

ACKNOWLEDGMENTS

The authors gratefully acknowledge the financial support from the National Natural Science Foundation of China (No. 22075237), the Natural Science Foundation of Fujian Province of China (No. 2020J01007), and the Shenzhen Basic Research Program (No. JCYJ20190809161407424).

[1] A. Noori, M. F. El-Kady, M. S. Rahmanifar, R. B. Kaner, and M. F. Mousavi, Towards establishing standard performance metrics for batteries, supercapacitors and beyond, Chem. Soc. Rev. **48**, 1272 (2019).

[2] Y. Guo, T. Park, J. W. Yi, J. Henzie, J. Kim, Z. Wang, B. Jiang, Y. Bando, Y. Sugahara, J. Tang, and Y. Yamauchi, Nanoarchitectonics for transition-metal-sulfide-based electrocatalysts for water splitting, Adv. Mater. **31**, 1807134 (2019).

[3] Y. Liu, C. Yang, Q. Zhang, and M. Liu, Recent progress in the design of metal sulfides as anode materials for sodium ion batteries, Energy Storage Mater. **22**, 66 (2019).

[4] M. R. Benzigar, V. D. B. C. Dasireddy, X. Guan, T. Wu, and G. Liu, Advances on emerging materials for flexible supercapacitors: Current trends and beyond, Adv. Funct. Mater. **30**, 2002993 (2020).

[5] Y. Zhou, C.-H. Wang, W. Lu, and L. Dai, Recent advances in fiber-shaped supercapacitors and lithium-ion batteries, Adv. Mater. **32**, 1902779 (2020).

[6] P. Pal and A. Ghosh, Three-Dimensional $CsPbCl_3$ Perovskite Anode for Quasi-Solid-State Li-Ion and Dual-Ion Batteries: Mechanism of Li^+ Conversion Process in Perovskite, Phys. Rev. Appl. **14**, 064010 (2020).

[7] C. Lian, M. Janssen, H. Liu, and R. van Roij, Blessing and Curse: How a Supercapacitor's Large Capacitance Causes its Slow Charging, Phys. Rev. Lett. **124**, 076001 (2020).

[8] A. A. Lee, D. Vella, A. Goriely, and S. Kondrat, Capacitance-Power-Hysteresis Trilemma in Nanoporous Supercapacitors, Phys. Rev. X **6**, 021034 (2016).

[9] N. C. Osti, B. Dyatkin, M. W. Thompson, F. Tiet, P. Zhang, S. Dai, M. Tyagi, P. T. Cummings, Y. Gogotsi, D. J. Wesolowski, and E. Mamontov, Influence of humidity on performance and microscopic dynamics of an ionic liquid in supercapacitor, Phys. Rev. Mater. **1**, 035402 (2017).

[10] J. Sun, C. Wu, X. Sun, H. Hu, C. Zhi, L. Hou, and C. Yuan, Recent progresses in high-energy-density all pseudocapacitive-electrode-materials-based asymmetric supercapacitors, J. Mater. Chem. A **5**, 9443 (2017).

[11] Y. He, B. Matthews, J. Wang, L. Song, X. Wang, and G. Wu, Innovation and challenges in materials design for flexible rechargeable batteries: From 1D to 3D, J. Mater. Chem. A **6**, 735 (2018).

[12] M. Kandasamy, A. Seetharaman, B. Chakraborty, I. Manohara Babu, J. J. William, G. Muralidharan, K. Jothivenkatachalam, and D. Sivasubramanian, Experimental and Theoretical Investigation of the Energy-Storage Behavior of a Polyaniline-Linked Reduced-Graphene-Oxide-SnO_2 Ternary Nanohybrid Electrode, Phys. Rev. Appl. **14**, 024067 (2020).

[13] Y. Shao, M. F. El-Kady, J. Sun, Y. Li, Q. Zhang, M. Zhu, H. Wang, B. Dunn, and R. B. Kaner, Design and mechanisms of asymmetric supercapacitors, Chem. Rev. **118**, 9233 (2018).

[14] T. Lv, Y. Yao, N. Li, and T. Chen, Wearable fiber-shaped energy conversion and storage devices based on aligned carbon nanotubes, Nano Today **11**, 644 (2016).

[15] X. Cai, C. Zhang, S. Zhang, Y. Fang, and D. Zou, Application of carbon fibers to flexible, miniaturized wire/fiber-shaped energy conversion and storage devices, J. Mater. Chem. A **5**, 2444 (2017).

[16] L. Huang, D. Santiago, P. Loyselle, and L. Dai, Graphene-based nanomaterials for flexible and wearable supercapacitors, Small **14**, 1800879 (2018).

[17] Y. Zhao, L. P. Wang, M. T. Sougrati, Z. Feng, Y. Leconte, A. Fisher, M. Srinivasan, and Z. Xu, A review on design strategies for carbon based metal oxides and sulfides nanocomposites for high performance Li and Na ion battery anodes, Adv. Energy Mater. **7**, 1601424 (2017).

[18] Z. Mustafa, D. Pravarthana, B. Wang, H. Yang, and R.-W. Li, Manipulation of Exchange Bias Effect via All-Solid-State Li-Ion Redox Capacitor with Antiferromagnetic Electrode, Phys. Rev. Appl. **14**, 014062 (2020).

[19] X. Y. Yu and X. W. Lou, Mixed metal sulfides for electrochemical energy storage and conversion, Adv. Energy Mater. **8**, 1701592 (2018).

[20] X. Han, G. Xiao, Y. Wang, X. Chen, G. Duan, Y. Wu, X. Gong, and H. Wang, Design and fabrication of conductive polymer hydrogels and their applications in flexible supercapacitors, J. Mater. Chem. A **8**, 23059 (2020).

[21] N. R. Hemanth and B. Kandasubramanian, Recent advances in 2D MXenes for enhanced cation intercalation in energy harvesting applications: A review, Chem. Eng. J. **392**, 123678 (2020).

[22] Y. Fang, D. Luan, and X. W. Lou, Recent advances on mixed metal sulfides for advanced sodium-ion batteries, Adv. Mater. **32**, 2002976 (2020).

[23] Q. Liu, X. Hong, X. Zhang, W. Wang, W. Guo, X. Liu, and M. Ye, Hierarchically structured Co_9S_8@$NiCo_2O_4$ nanobrushes for high-performance flexible asymmetric supercapacitors, Chem. Eng. J. **356**, 985 (2019).

[24] C. Sevik and D. Çakır, Tailoring Storage Capacity and Ion Kinetics in Ti_2CO_2/Graphene Heterostructures by Functionalization of Graphene, Phys. Rev. Appl. **12**, 014001 (2019).

[25] J. Liu, J. Wang, C. Xu, H. Jiang, C. Li, L. Zhang, J. Lin, and Z. X. Shen, Advanced energy storage devices: Basic principles, analytical methods, and rational materials design, Adv. Sci. **5**, 1700322 (2018).

[26] V. Augustyn, J. Come, M. A. Lowe, J. W. Kim, P.-L. Taberna, S. H. Tolbert, H. D. Abruna, P. Simon, and B. Dunn, High-rate electrochemical energy storage through Li^+ intercalation pseudocapacitance, Nat. Mater. **12**, 518 (2013).

[27] G. Shao, R. Yu, X. Zhang, X. Chen, F. He, X. Zhao, N. Chen, M. Ye, and X. Y. Liu, Making stretchable hybrid supercapacitors by knitting non-stretchable metal fibers, Adv. Funct. Mater. **30**, 2003153 (2020).

[28] Q. Liu, X. D. Hong, X. Y. You, X. Zhang, X. Zhao, X. Chen, M. D. Ye, and X. Y. Liu, Designing heterostructured metal sulfide core-shell nanoneedle films as battery-type electrodes for hybrid supercapacitors, Energy Storage Mater. **24**, 541 (2020).

[29] X. Zhang, X. Chen, T. Bai, J. Chai, X. Zhao, M. Ye, Z. Lin, and X. Liu, A simple route to fiber-shaped heterojunctioned nanocomposites for knittable high-performance supercapacitors, J. Mater. Chem. A **8**, 11589 (2020).

[30] X. Zhao, X. Zhang, W. Wang, T. Bai, X. Chen, and M. Ye, Comparative study on electrochemical charge storage behavior of $FeCo_2S_4$ electrodes with different dimensional nanostructures, Appl. Phys. Lett. **116**, 193901 (2020).

[31] Y. Liu, Y. Li, H. Kang, T. Jin, and L. Jiao, Design, synthesis, and energy-related applications of metal sulfides, Mater. Horiz. **3**, 402 (2016).

[32] X. Y. Yu, L. Yu, and X. W. D. Lou, Metal sulfide hollow nanostructures for electrochemical energy storage, Adv. Energy Mater. **6**, 1501333 (2016).

[33] X. Chen, Q. Liu, T. Bai, W. Wang, F. He, and M. Ye, Nickel and cobalt sulfide-based nanostructured materials for electrochemical energy storage devices, Chem. Eng. J. **409**, 127237 (2020).

[34] P. Guo, H. Song, Y. Liu, and C. Wang, $CuFeS_2$ quantum dots anchored in carbon frame: Superior lithium storage performance and the study of electrochemical mechanism, ACS Appl. Mater. Interfaces **9**, 31752 (2017).

[35] Y. Tan, W.-D. Xue, Y. Zhang, D.-X. He, W.-J. Wang, and R. Zhao, Solvothermal synthesis of hierarchical alpha-NiS particles as battery-type electrode materials for hybrid supercapacitors, J. Alloys Compd. **806**, 1068 (2019).

[36] X. Wang, Q. Zhang, J. Sun, Z. Zhou, Q. Li, B. He, J. Zhao, W. Lu, C.-p. Wong, and Y. Yao, Facile synthesis of hierarchical porous manganese nickel cobalt sulfide nanotube arrays with enhanced electrochemical performance for ultrahigh energy density fiber-shaped asymmetric supercapacitors, J. Mater. Chem. A **6**, 8030 (2018).

[37] V. K. Mariappan, K. Krishnamoorthy, P. Pazhamalai, S. Sahoo, S. S. Nardekar, and S.-J. Kim, Nanostructured ternary metal chalcogenide-based binder-free electrodes for high energy density asymmetric supercapacitors, Nano Energy **57**, 307 (2019).

[38] Z. Hao, X. He, H. Li, D. Trefilov, Y. Song, Y. Li, X. Fu, Y. Cui, S. Tang, H. Ge, and Y. Chen, Vertically aligned and ordered arrays of 2D MCo_2S_4@metal with ultrafast ion/electron transport for thickness-independent pseudocapacitive energy storage, ACS Nano **14**, 12719 (2020).

[39] J. Long, Z. Hou, C. Shu, C. Han, W. Li, R. Huang, and J.-Z. Wang, Free-standing 3D $CuCo_2S_4$ nanosheet array with high catalytic activity as an efficient oxygen electrode for lithium-oxygen batteries, ACS Appl. Mater. Interfaces **11**, 3834 (2019).

[40] W. Liu, J. Zhang, Z. Bai, G. Jiang, M. Li, K. Feng, L. Yang, Y. Ding, T. Yu, Z. Chen, and A. Yu, Controllable urchin-like $NiCo_2S_4$ microsphere synergized with sulfur-doped graphene as bifunctional catalyst for superior rechargeable Zn–air battery, Adv. Funct. Mater. **28**, 1706675 (2018).

[41] M. Li, X. Li, Z. Li, and Y. Wu, Hierarchical nanosheet-built $CoNi_2S_4$ nanotubes coupled with carbon-encapsulated carbon nanotubes@Fe_2O_3 composites toward high-performance aqueous hybrid supercapacitor devices, ACS Appl. Mater. Interfaces **10**, 34254 (2018).

[42] W. Lu, M. Yang, X. Jiang, Y. Yu, X. Liu, and Y. Xing, Template-assisted synthesis of hierarchically hollow $C/NiCo_2S_4$ nanospheres electrode for high performance supercapacitors, Chem. Eng. J. **382**, 122943 (2020).

[43] Q. Li, W. Lu, Z. Li, J. Ning, Y. Zhong, and Y. Hu, Hierarchical $MoS_2/NiCo_2S_4$@C urchin-like hollow microspheres for asymmetric supercapacitors, Chem. Eng. J. **380**, 122544 (2020).

[44] See Supplemental Material at http://link.aps.org/supplemental/10.1103/PhysRevApplied.15.064042 for the schematic illustrations of the growth processing for various hierarchical $NiCo_2S_4$ microstructures, FTIR spectra of different materials, XRD patterns of different materials, N_2 absorption-desorption isotherm curves and distribution plots of pore sizes of the brushlike $NiCo_2S_4$ and flowerlike $NiCo_2S_4$, tables containing some parameters of the four $NiCo_2S_4$ hierarchical structures, the resistance parameters of the four $NiCo_2S_4$ electrodes and the performance comparison of different $NiCo_2S_4$ electrodes, and energy dispersive spectroscopy results of the four $NiCo_2S_4$ electrodes, respectively.

[45] X. Hong, Q. Liu, X. Gao, C. He, X. You, X. Zhao, X. Liu, and M. Ye, Rational design of coralloid Co_9S_8-CuS hierarchical architectures for quantum dot-sensitized solar cells, J. Mater. Chem. A **6**, 11384 (2018).

[46] C. Chen, M. Ye, N. Zhang, X. Wen, D. Zheng, and C. Lin, Preparation of hollow Co_9S_8 nanoneedle arrays as effective counter electrodes for quantum dot-sensitized solar cells, J. Mater. Chem. A **3**, 6311 (2015).

[47] Y. Ruan, C. Wang, and J. Jiang, Nanostructured Ni compounds as electrode materials towards high-performance electrochemical capacitors, J. Mater. Chem. A **4**, 14509 (2016).

[48] M. Liu, Q. Wang, Z. Liu, Y. Zhao, X. Lai, J. Bi, and D. Gao, In-situ N-doped $MnCO_3$ anode material via one-step solvothermal synthesis: Doping mechanisms and enhanced electrochemical performances, Chem. Eng. J. **383**, 123161 (2020).